

## Validating continuous digital light processing (cDLP) additive manufacturing accuracy and tissue engineering utility of a dye-initiator package

This content has been downloaded from IOPscience. Please scroll down to see the full text.

2014 Biofabrication 6 015003

(<http://iopscience.iop.org/1758-5090/6/1/015003>)

View [the table of contents for this issue](#), or go to the [journal homepage](#) for more

Download details:

IP Address: 130.60.206.75

This content was downloaded on 06/01/2015 at 20:17

Please note that [terms and conditions apply](#).

# Validating continuous digital light processing (cDLP) additive manufacturing accuracy and tissue engineering utility of a dye-initiator package

Jonathan Wallace<sup>1</sup>, Martha O Wang<sup>2</sup>, Paul Thompson<sup>3,8</sup>, Mallory Busso<sup>3</sup>,  
Vaijayantee Belle<sup>3,9</sup>, Nicole Mammoser<sup>3</sup>, Kyobum Kim<sup>2,10</sup>,  
John P Fisher<sup>4</sup>, Ali Siblani<sup>5</sup>, Yueshuo Xu<sup>3</sup>, Jean F Welter<sup>6</sup>,  
Donald P Lennon<sup>6</sup>, Jiayang Sun<sup>7</sup>, Arnold I Caplan<sup>6</sup> and David Dean<sup>3,11,12</sup>

<sup>1</sup> Department of Biomedical Engineering, Case Western Reserve University, Cleveland, OH 44106, USA

<sup>2</sup> Department of Chemical and Biomolecular Engineering, University of Maryland, College Park, MD 20742, USA

<sup>3</sup> Department of Neurological Surgery, Case Western Reserve University, Cleveland, OH 44106, USA

<sup>4</sup> Fischell Department of Bioengineering, University of Maryland, College Park, MD 20742, USA

<sup>5</sup> EnvisionTEC, Inc., 15162 South Commerce Drive, Dearborn, MI 48120, USA

<sup>6</sup> Department of Biology, Case Western Reserve University, Cleveland, OH 44106, USA

<sup>7</sup> Department of Epidemiology and Biostatistics, Case Western Reserve University, Cleveland, OH 44106, USA

E-mail: [Jonathan.Wallace@Case.Edu](mailto:Jonathan.Wallace@Case.Edu), [martha@umd.edu](mailto:martha@umd.edu), [Paul.M.Thompson@Case.Edu](mailto:Paul.M.Thompson@Case.Edu),  
[Mallory.Busso@Case.Edu](mailto:Mallory.Busso@Case.Edu), [Vaijayantee.Belle@gmail.com](mailto:Vaijayantee.Belle@gmail.com), [Nicole.Mammoser@Case.Edu](mailto:Nicole.Mammoser@Case.Edu),  
[kyk24@pitt.edu](mailto:kyk24@pitt.edu), [jpfisher@umd.edu](mailto:jpfisher@umd.edu), [asiblani@envisiontec.com](mailto:asiblani@envisiontec.com), [Yueshuo.Xu@Case.Edu](mailto:Yueshuo.Xu@Case.Edu),  
[jfw2@case.edu](mailto:jfw2@case.edu), [Donald.Lennon@Case.Edu](mailto:Donald.Lennon@Case.Edu), [jsun@case.edu](mailto:jsun@case.edu), [Arnold.Caplan@Case.Edu](mailto:Arnold.Caplan@Case.Edu) and  
[David.Dean@osumc.edu](mailto:David.Dean@osumc.edu)

Received 2 April 2013, revised 2 October 2013

Accepted for publication 4 October 2013

Published 15 January 2014

## Abstract

This study tested the accuracy of tissue engineering scaffold rendering via the continuous digital light processing (cDLP) light-based additive manufacturing technology. High accuracy (i.e.,  $<50\ \mu\text{m}$ ) allows the designed performance of features relevant to three scale spaces: cell-scaffold, scaffold-tissue, and tissue-organ interactions. The biodegradable polymer poly(propylene fumarate) was used to render highly accurate scaffolds through the use of a dye-initiator package,  $\text{TiO}_2$  and bis (2,4,6-trimethylbenzoyl)phenylphosphine oxide. This dye-initiator package facilitates high accuracy in the Z dimension. Linear, round, and right-angle features were measured to gauge accuracy. Most features showed accuracies between 5.4–15% of the design. However, one feature, an  $800\ \mu\text{m}$  diameter circular pore, exhibited a 35.7% average reduction of patency. Light scattered in the  $x, y$  directions by the dye may have reduced this feature's accuracy. Our new fine-grained understanding of accuracy could be used to make further improvements by including corrections in the scaffold design software. Successful cell attachment occurred with both canine and human mesenchymal stem cells (MSCs). Highly accurate cDLP scaffold rendering is critical to the design of scaffolds

<sup>8</sup> Present address: School of Medicine, Duke University, Durham, NC 27710, USA.

<sup>9</sup> Present address: Department of Neurology, Tufts Medical Center, Boston, MA 02111, USA.

<sup>10</sup> Present address: Department of Bioengineering, University of Pittsburgh, Pittsburgh, PA 15261, USA.

<sup>11</sup> Present address: Department of Plastic Surgery, Ohio State University, Columbus, OH 43210, USA.

<sup>12</sup> Author to whom any correspondence should be addressed.

that both guide bone regeneration and that fully resorb. Scaffold resorption must occur for regenerated bone to be remodeled and, thereby, achieve optimal strength.

(Some figures may appear in colour only in the online journal)

## 1. Introduction

Much attention has been given recently to the additive manufacturing [1] of resorbable, porous, polymeric tissue engineering scaffolds [2, 3, 4]. Light-based additive manufacturing of tissue engineered resorbable scaffolds for critical size [5] and larger wounds now appears to be possible with accuracy of less than 50  $\mu\text{m}$ . This level of accuracy opens the possibility of designing scaffold performance at three critical scale-spaces: cell-scaffold, scaffold-tissue, and tissue-organ. We have experience with two highly accurate additive manufacturing technologies for the light-based polymerization of resorbable tissue engineering scaffolds: stereolithography [6, 7] and continuous digital light processing (cDLP) (figure 1(A)) [8, 9, 10].

### 1.1. Continuous digital light processing (cDLP)

Polymeric tissue engineering scaffolds rendered from low molecular weight polymers (i.e., low molecular weight ( $M_n$ ) < 4000 Daltons (Da)) are more likely to facilitate cell attachment and proliferation, host incorporation, scaffold resorption, and tissue regeneration [4]. cDLP-based additive manufacturing devices from envisionTEC (Ferndale, MI) utilize a DLP® (Texas Instruments [TI], Dallas, TX) chip. The DLP chip includes a TI digital micromirror device (DMD) chip which in the envisionTEC Perfactory® device is used to project each layer through a translucent basement plate, or 'build basement', above which sits a polymer-based resin and a 'build platform' attached to an elevator (figure 1(A)). The DMD chip consists of an array of micro-mirrors which can separately control the intensity of projected UV light at each pixel of the layer image, thereby simultaneously controlling the polymerization of each voxel (volumetric pixel) within a layer. Indeed, the term 'continuous' DLP (cDLP) refers to the continuous curing of all voxels in a layer.

### 1.2. cDLP additive manufacturing system for rendering tissue engineering scaffolds

The cDLP scaffold additive manufacturing system that we have developed uses the resorbable polymer, poly(propylene fumarate) (PPF), and a commercial cDLP additive manufacturing device. The strength of the resulting scaffolds will be affected by the polymer's (i.e., PPF) molecular weight. Because of its high viscosity, the monomer precursor to PPF, diethyl fumarate (DEF), is used as a solvent. The ratio of polymer and solvent used will also affect cross-linking density, and therefore the stiffness, of the resulting scaffolds [11]. A dye-initiator package is used to ensure accurate control of the depth of polymerization (i.e., 'Z' resolution). After much research into biocompatible dyes [9], in the study reported

here we chose titanium dioxide ( $\text{TiO}_2$ ) as the dye ('dye' is used here for consistency; technically,  $\text{TiO}_2$  is a pigment, not a dye, since it is insoluble and held in suspension) and BAPO as the initiator.

$\text{TiO}_2$  has a high index of refraction—in the rutile form it is approximately 2.7—and, thus, it prevents UV light penetration through scattering. The Perfactory P3 device UV output spectrum is in the 350–430 nm range with a peak at 380 nm. The choice of dye and initiator should be based on this output range, as both must be active in this region. As noted in figure 2, the peak absorbance of  $\text{TiO}_2$  begins to drop off at 350 nm whereas the two peak absorbances for BAPO are at 340 and 380 nm [12]. We have previously documented the photoreactivity of PPF in the presence of BAPO [11, 13, 14]. Note that it is important that the peak absorbance of the dye not supersede that of the initiator. Once an appropriate  $\text{TiO}_2$  concentration was found, BAPO concentration did not have a significant effect on layer thickness, however, exposure time can be used effectively to control the depth of curing.

Toxicity would be a concern were the dyes used for current commercial (i.e., non-implantable) cDLP additive manufacturing used in tissue engineering applications. It was also important to us during this preclinical research that all resin components, since they would be incorporated into the implant, could be readily obtained from sources that guarantee the material's safety as per governing FCC and/or USP regulations. In our initial testing of PPF for cDLP photoinitiation, we used a rapid prototyping industry standard azo chromium dye [9, 10]. However, this dye is not intended for internal use. We next investigated the use of two antibiotics, doxycycline hyclate and amphotericin B, as dyes [9, 10]. Incorporation of antibiotics may be useful, however the primary goal in using these dyes was to control depth of polymerization to achieve 70–100  $\mu\text{m}$  overcuring between layers, termed 'stitching', while building in 50  $\mu\text{m}$  layers. This level of overcuring prevents delamination during the initial build. This level of accuracy allows the design of scaffold performance at three different scale spaces that are discussed in sections 1.3–1.5. Thus, our choice of  $\text{TiO}_2$  solves both of our demands of a dye, sufficient attenuation of light and that it is in production for FDA-approved food and drug applications [15]. Moreover, both the rutile and anatase versions of  $\text{TiO}_2$  have been shown to promote osseointegration of medical implants [16].

### 1.3. Cell-scaffold interactions

Cell-scaffold interactions may be strongly impacted by polymerization chemistry. Potential impacts include the scaffold's surface features and resorption chemistry. It is essential that polymerization chemistry (a) not incorporate free monomer (i.e., DEF) or unpolymerized polymer (i.e.,

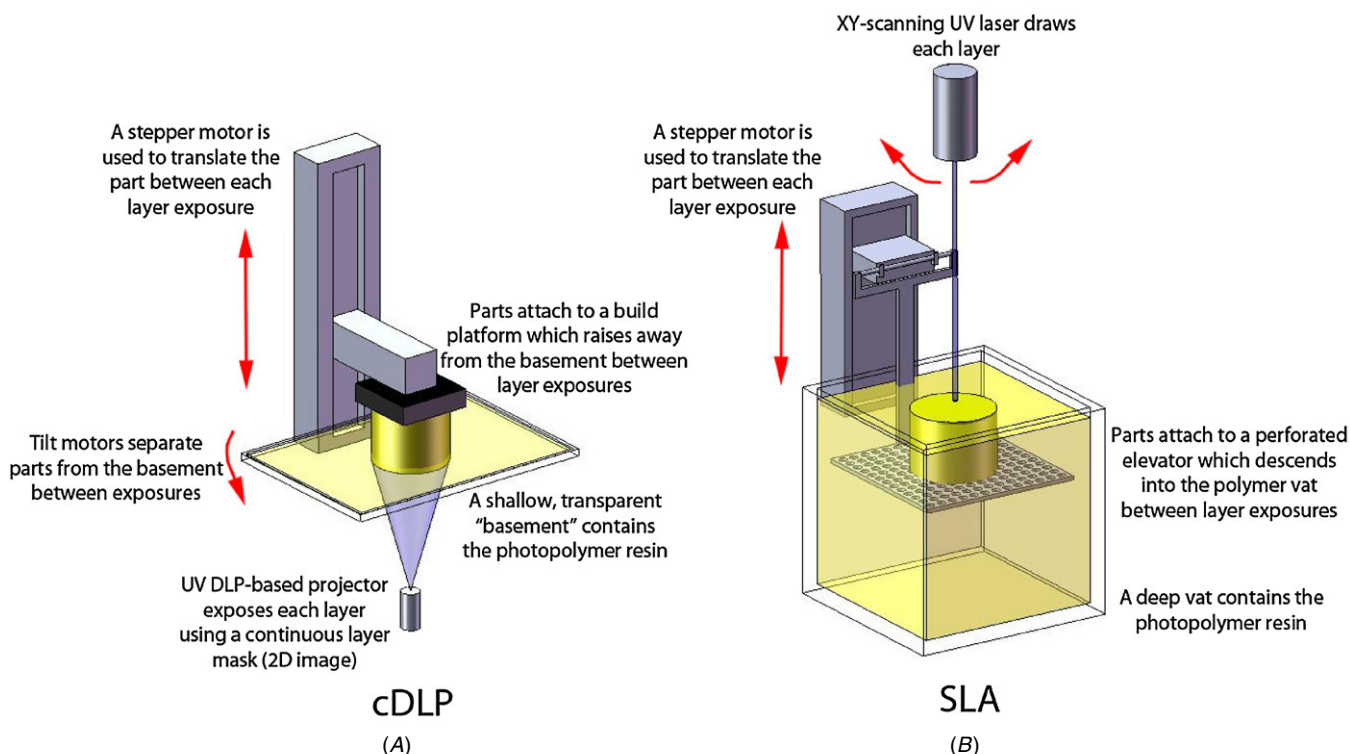


**Figure 1.** Both (A) continuous digital light processing (cDLP) and (B) stereolithography (SLA) additive manufacturing systems rely on photocrosslinking. However, the methods differ as illustrated here. cDLP uses a UV projector to expose each layer continuously (i.e., all areas simultaneously). SLA utilizes a UV laser to draw each cross-section, or layer. SLA typically requires a vat of resin. As parts are built, they attach to a perforated elevator which moves further down into the vat of resin as each layer is rendered at the surface. In contrast, cDLP systems render parts by projecting each image through a clear basement containing the resin, curing at the bottom surface rather than the top surface. The parts attach to a build platform which moves upward, out of the resin, after each layer is projected. Before the part is put back into position for the next layer to be projected, tilt motors peel the basement away from a newly cured layer to insure clean separation.

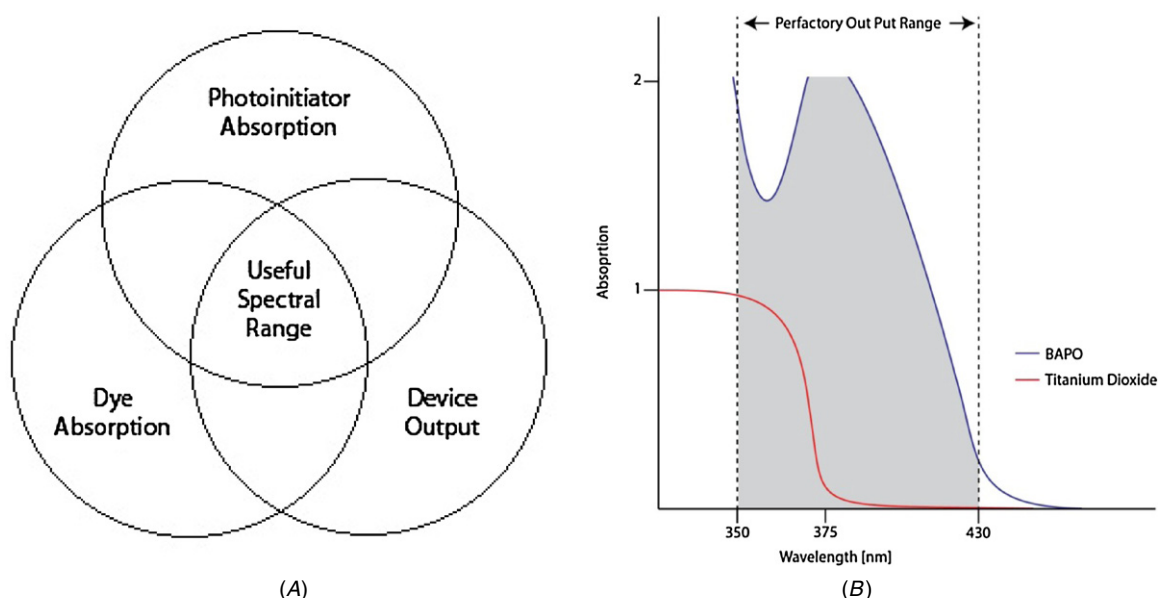


**Figure 2.** Relationship of dye and initiator. (A). It is essential that the pairing of dye and initiator, or 'dye-initiator package', correspond to the device output spectrum. For polymerization to occur, the absorption spectrum of the photoinitiator must overlap with the device output range. Similarly, a dye will only be effective in controlling the depth of polymerization if it blocks (i.e., absorbs and/or scatters) light in this range. (B). The region shaded in gray illustrates the wavelengths at which the spectra of this dye-initiator package (i.e., TiO<sub>2</sub>/BAPO) and the device output spectrum overlap.

PPF) as both may impact cell viability (cell viability <3% for uncrosslinked networks versus >80% for crosslinked networks) [17, 18] and (b) results in an implant with sufficient 'green strength' to allow post-rendering cleaning of unpolymerized polymer from the scaffold's pores [8, 9].

In addition to chemistry and material properties, scaffold shape can affect cell-scaffold and general environment-scaffold interactions. Computer aided design (CAD) software can incorporate features of post-polymerization shrinkage (i.e., following initial scaffold rendering) and swelling due to wetting (e.g., during *in vitro* pre-implantation bioreactor culturing and/or *in vivo* post-implantation) to produce a scaffold that accurately matches the original CAD dimensions. Cell-scaffold interactions, polymerization chemistry, scaffold material properties, scaffold shape, and other features that affect scaffold strength and rigidity can provide information that is useful for scaffold resorption kinetics modeling.

Finally, the initial goal of host or stem cell seeding is cell attachment to the scaffold [19]. PPF's hydrophobic surface can be modified through radiofrequency glow-discharge (RFGD) or by soaking the implant in serum which leads to protein adsorption [20, 21]. Cell attachment can also be mediated by embedding substances in the surface that mimic extracellular matrix components. In the case of osteoblasts, this includes surface roughness at nm [22] and/or  $\mu\text{m}$  [23, 24] sizes as well as the material's compliance [25, 26]. Once the initial goal of attachment has occurred, optimal surface properties may need to promote cell proliferation and eventually maturation as host tissue integrates the construct. Cell-scaffold interactions may also be affected by mechanical forces applied by the surrounding environment. For example, those forces could include pre-implantation culturing of a scaffold in a bioreactor where media flow exerts shear forces on seeded cells [27, 28].

#### 1.4. Scaffold-tissue interactions

It is critical to the regeneration of many tissues that scaffolds resorb in response to cell maturation and the integration of host tissue. Well-timed, predictable scaffold resorption kinetics are important in avoiding problems such as premature or rapid loss of material properties, bulk degradation, or an acidic spike that has been observed with large polylactide-based implants [29, 30]. Predictable scaffold resorption is also necessary for the successful integration of vasculature, unfettered remodeling, and host incorporation of neotissue. The incorporation of tricalcium phosphate into resorbable polymer scaffolds is expected to buffer the pH of resorbing scaffolds [31], and it may also affect surface roughness properties.

The geometry of internal porous scaffold spaces is also critical to the loading of cells and the establishment of vascular channels [2, 32–34]. Effective pores and channels are likely to be between 150  $\mu\text{m}$ –1 mm in diameter. These interactions (i.e., tissue maturation and vascular infusion) at this scaffold-tissue scale-space occur over days to months as opposed to the s to h long events in the cell-scaffold scale-space. There may also be strain distributions resulting from activity surrounding

or involving the defect site following scaffold implantation [12, 28]. It is therefore important to compensate in the computer aided design of scaffold shapes to correct for anisotropic shrinkage due to support structure and scaffold geometry, post-curing shrinkage of implants, as well as swelling due to wetting caused by pre-implantation cell culturing or implantation itself.

#### 1.5. Tissue-organ interactions

In addition to the scaffold design parameters affecting the cellular and tissue scale-spaces, scaffold design must include an external shape that accurately fits the patient-specific, defect site in the damaged organ. For example, it may be necessary to have infusion channels opening toward the host tissue in the defect site to allow tissue ingrowth prior to the implant's full degradation. The relevant scale space on this level is likely 100's of  $\mu\text{m}$  to mm.

Scaffold design features, such as wall thickness, affect the macro strain distribution and may be optimized to resist trauma [35]. Moreover, it may be necessary to counterbalance desired resorption processes with the need for the implant to be mechanically loaded during tissue regeneration. The need to at least temporarily localize strain-bearing to portions of a scaffold or surrounding fixation devices may necessitate the consideration of protection sited outside the body (e.g., a helmet or a limb-surrounding cast). Alternatively, it may be useful to have internal strain-bearing regions. It is possible that these regions may be subsequently removed in order to avoid long-term stress-shielding. These structures may be on the order of mm to cm and the processes involved may occur over periods of days, to months, to a lifetime.

## 2. Materials and methods

### 2.1. Preparation of PPF

Poly(propylene fumarate) (PPF) was synthesized using a two-step process described previously [36]. Briefly, diethyl fumarate (DEF) (Acros, Pittsburgh PA) is reacted with propylene glycol (Acros) in a 1:3 molar ratio with zinc chloride (Sigma Aldrich, St. Louis, MO) and hydroquinone (Sigma Aldrich) as a catalyst and a crosslinking inhibitor, respectively. This first step produces an intermediate, bis(hydroxypropynol) and ethanol as a byproduct. In the second step the intermediate undergoes transesterification under a vacuum and PPF is produced with propylene glycol as the byproduct. The PPF is then purified and gel permeation chromatography is performed to determine the number average molecular weight ( $M_n$ ).

### 2.2. Preparation of scaffold resin for cDLP

PPF with a molecular weight ( $M_n$ ) of 1200 Da was used for this study. DEF was added in a mass ratio of 1:2 DEF: PPF for test scaffolds, and 1:1 DEF:PPF for full size scaffolds. Increasing the proportion of DEF to PPF, from 1:2 to 1:1, was necessitated by the increase in resin viscosity due to crosslinking of the material, which occurred slowly throughout



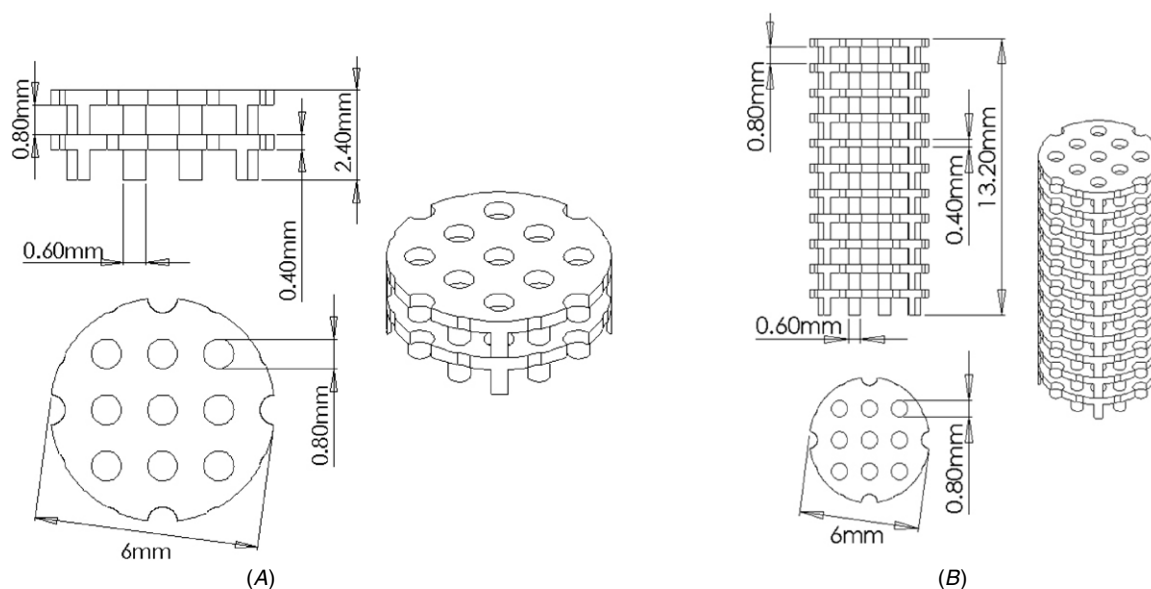


**Figure 3.** The test ‘plate and post’ scaffold design. (A) reduced-size ‘test’ scaffold designed to accelerate testing. The part consists of two 400  $\mu\text{m}$  thick plates separated by 800  $\mu\text{m}$  posts which are 600  $\mu\text{m}$  in diameter. 800  $\mu\text{m}$  diameter circular channels perforate the plates. A 6 mm overall scaffold diameter was used. A separate set of posts at the base of the scaffold are used for supports during the build process. (B) The full, implantable, ‘plate and post’ scaffold. Internal pore geometries are the same as those for the test scaffold. The overall dimensions of the scaffold, 6 mm in diameter with a 12.4 mm height, are well suited for mechanical compression testing, *in vitro* research, and *in vivo* research. Note that the dimensions shown in the figure are in millimeters.

the calibration process. The photoinitiator BAPO (BASF [Ciba], Ludwigshafen, Germany) was added in a concentration of 5, 10, or 20  $\text{mg g}^{-1}$  of combined PPF/DEF resin mass. The  $\text{TiO}_2$  concentrations utilized during calibration varied from 0–48  $\text{mg TiO}_2/\text{g}$  of PPF/DEF. Rutile  $\text{TiO}_2$  with an average particle size of 300 nm (Sachtleben, Duisburg, Germany) was used. In combining the components listed here, a particular order was useful to expedite the mixing process and more quickly achieve homogeneity of the resin. BAPO was first added to DEF, which is of much lower viscosity than PPF, and was mixed until thoroughly dissolved. The PPF was then heated to lower its viscosity before adding the DEF/BAPO mixture. Care was taken to avoid excessive temperatures ( $>70^\circ\text{C}$ ) which could cause the polymer to cross-link. Once the PPF/DEF/BAPO mixture was prepared,  $\text{TiO}_2$  was added in incremental steps to allow for calibration of curing parameters as a function of  $\text{TiO}_2$  concentration.

### 2.3. Curing tests for layer thickness calibration

The cDLP-based additive manufacturing device used for this study was the Perfactory<sup>®</sup> P3 Mini Multi Lens (envisionTEC, Dearborn, MI), which was operated in UV mode. The device was configured with a 75 mm focal length lens, providing a native in-plane (i.e., XY) resolution of 42  $\mu\text{m}$  (21  $\mu\text{m}$  effective resolution using the ‘enhanced resolution module’ or ERP). The between-plane (i.e., Z) resolution used was 50  $\mu\text{m}$ . Curing tests were performed to determine the relationship between  $\text{TiO}_2$  concentration, BAPO concentration, and cured layer thickness. To perform each test, a few drops of resin were placed on a glass slide. The Perfactory P3 device was used to cure the resin with a fixed irradiance and time using an

11 mm, square-shaped test pattern. A 200  $\text{mW dm}^{-2}$  irradiance and an exposure time of either 60 or 300 s was used for these tests. An additional calibration was needed for the added thickness of the glass slide. After the specified time period had elapsed, the excess uncured polymer was removed from the slide leaving only the solid square test pattern. A razor blade was then used to remove the thin layer from the slide, and digital calipers (Model 500–171–20, Mitutoyo America Corp., Aurora, IL) were used to measure the thickness of the layer. Three replicates were performed for each unique combination of BAPO and  $\text{TiO}_2$  concentration evaluated.

### 2.4. cDLP additive manufacturing of test and full-size scaffolds

The ‘plate and post’ pore geometry used in our test and full scaffold geometries is based on a design developed by Cooke [37] that is intended to guide the regeneration of cranial bone. Geometric models of this design were developed using SolidWorks<sup>®</sup> (Dassault Systèmes SolidWorks Corp., Waltham, MA) software, and are illustrated in figure 3. A modified version of a full sized scaffold, a test scaffold (figure 3(A)), was developed to reduce initial testing time.

A successful build begins with curing ten 50  $\mu\text{m}$  layers of resin over the entire build area, what is referred to as a ‘burn-in patch’. In some cases set up of the burn-in patch benefitted from additional curing outside of the Perfactory device.

Test and full-size scaffolds were built using a 200  $\text{mW dm}^{-2}$  irradiance and a 150 s exposure time. This exposure time was chosen after it was determined that 150 s produced an appropriate layer thickness with greater

**Table 1.** 2-plate test scaffold accuracy: plate diameter measurements. Resin was prepared using a 2:1 PPF/DEF ratio and containing 2 wt% BAPO and 1 wt% TiO<sub>2</sub>. From this material, four 2-plate test scaffolds (figure 2(A)) were rendered. A 150 s exposure time and a 200 mW dm<sup>-2</sup> irradiance were used. For each test scaffold, the plate diameter was measured using digital calipers. The expected diameter was 6.0 mm. The observed error is approximately twice the Perfactory device's native XY resolution of 42  $\mu$ m. \*This plate was damaged during post-processing and could not be measured.

Sample number	Plate 1 diameter (mm)	Plate 2 diameter (mm)
1	5.90	N/A*
2	6.02	5.83
3	5.93	5.94
4	5.97	5.84
Average		5.92
Standard deviation		0.12

strength than a 60 s exposure with a reasonably fast build time. The build process was paused once per hour to allow the resin to be mixed, ensuring a homogeneous suspension of TiO<sub>2</sub> particles. While paused, any extraneous material adhering to the basement in regions of 'dark curing' (i.e., where light had not been projected) was removed.

Post-processing of the scaffolds was necessary to remove any uncured resin. The build platform, burn-in patch, and the attached scaffolds were removed from the Perfactory and then rinsed with 100% ethanol and then compressed air was used to remove any excess uncured resin from the internal pore spaces. Next, the build platform, burn-in patch, and scaffolds were placed in a UV bath (i.e., 'post-curing' in a ProCure™ 350, 3D Systems, Rock Hill, SC) for 2 h to ensure complete crosslinking. The burn-in patch was then separated from the build platform, and the individual scaffolds were removed from the burn-in patch by cutting supports connecting them to the burn-in patch with a razor blade. Support remnants were removed from the scaffolds with via fine sanding.

## 2.5. Post-cured specimen mechanical properties

We have previously reported the compressive modulus and fracture strength of photo-crosslinked PPF [38]. Those studies determined that heat release during photocuring and mechanical properties decline as the proportion of DEF:PPF increases from 50% DEF to 75% [39]. Since this had not been studied with TiO<sub>2</sub> present, five 10 mm diameter, 20 mm tall cylindrical specimens were prepared from a 1:1 PPF/DEF blend (PPF MW 1200 Da) with 1% BAPO and 1% TiO<sub>2</sub> on a Perfactory P3. Compressive modulus measurements were taken from these cylinders using an Instron (Norwood, MA) 8501 uniaxial testing machine.

## 2.6. Test scaffold rendering accuracy

Initially reduced-size 'test' scaffold plates (see figure 3 for 'plate and post' design) were produced and measured (table 1) using digital calipers (Mitutoyo, Model 500–171–20).

## 2.7. Full scaffold rendering accuracy

Once the fabrication process had been calibrated, our goal was to measure distance (linear) and shape features on full-size scaffolds. Shrinkage was expected in linear distance measures. If this shrinkage was significantly anisotropic, it would have an effect on the geometric accuracy of the scaffolds. To assess geometric accuracy we measured the accuracy of round and square features. Round features were assessed with a curvature measurement and squared-off features with a perpendicular bisector.

In order to collect these measurements 16 full size scaffolds were imaged using micro computed tomography ( $\mu$ CT).  $\mu$ CT was performed using a SCANCO Medical (Brüttisellen, Switzerland)  $\mu$ CT 100 imaging system to nondestructively image and quantify scaffold parameters at 10  $\mu$ m isotropic (i.e., 10  $\mu$ m pixel size and slice thickness) resolution. The resulting image volumes were visualized in Amira® (Visage Imaging, San Diego, CA). The scaffold portion of the  $\mu$ CT image volumes were segmented from other material in the scan (e.g., the scanning platform) and aligned to allow orthogonal views of the cylindrical scaffolds. Software was written in MATLAB (MathWorks, Natick, MA) to facilitate the collection of lengths, curvatures, and perpendicular bisectors from these images. Complete scaffold length (figure 4(K)) and plate thickness of the 11 plates in each scaffold centrally and at the edge of all plates (figures 4(E) and (F)) were measured. Curvature measurements were taken to indicate the size and roundness of circular scaffold features (i.e., posts, plates, and pores: figures 4(B)–(D), respectively). There are 12 full posts between each pair of plates and nine pores in each plate. Perpendicular bisectors were used to measure the accuracy of the plate-post-junction which is expected to be a right angle (figures 4(G)–(L)). The plate-post-angle was measured at the top and bottom of posts, as with the plate thickness measurements, centrally and at the edge of all plates (figures 4(G)–(J)).

## 2.8. Human MSC seeding

Preliminary tests were made of the utility of the full-sized scaffolds as bone tissue engineering devices. Human bone marrow was obtained from consenting adult volunteers under an approved Institutional Review Board human subjects protocol. Primary cultures of isolated human mesenchymal stem cells (hMSCs) were seeded at 180 000 cells cm<sup>-2</sup> in 175 cm<sup>2</sup> tissue culture flasks until day 14 (i.e., before confluence). The primary isolates of hMSCs were sub-cultured at a density of 250 000 cells per culture flask with 10 ng ml<sup>-1</sup> fibroblastic growth factor-basic (FGF-2) (Peprotech, Rocky Hill, NJ). The hMSCs were trypsinized after seven days in first passage; cells were counted and a dense cell infusate was prepared with 32.5 million cells in 2 ml of Dulbecco's modified Eagle medium—low glucose (DMEM-LG) supplemented with 10 (v/v)% fetal bovine serum (FBS). Four PPF scaffolds were rendered, as described in section 2.4, and sterilized with ethylene oxide gas (37.8 °C), and pre-wetted by immersion in FBS for 12 h. The number of hMSCs loaded in each scaffold was 3.25 million (the optimal cell

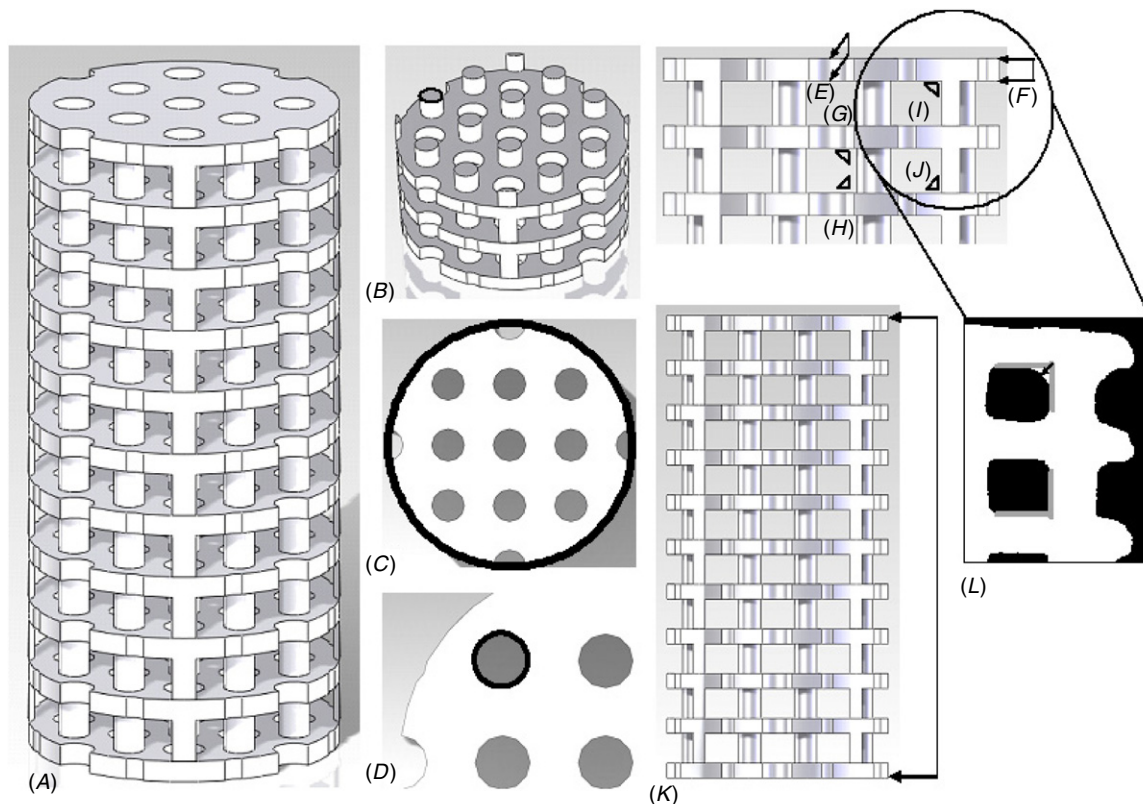


**Figure 4.**  $\mu$ CT linear and curved feature accuracy assessment: (A) Complete scaffold view. Circular features: (B) post curvature (expected measurement:  $3.33 \text{ mm}^{-1}$ ), (C) plate curvature ( $0.33 \text{ mm}^{-1}$ ), and (D) pore curvature ( $2.5 \text{ mm}^{-1}$ ). Length features: (E) inner plate thickness ( $0.4 \text{ mm}$ ), (F) outer (edge) plate thickness ( $0.4 \text{ mm}$ ), and (K) Scaffold height (expected:  $12.4 \text{ mm}$ ). Right angle features: (G) distance of expected post-plate vertex ( $0 \text{ mm}$ ) at top of a middle post/plate junction, (H) distance of expected post-plate vertex ( $0 \text{ mm}$ ) at bottom of a middle post/plate junction, (I) distance of expected post-plate vertex ( $0 \text{ mm}$ ) at top of an edge post/plate junction, and (J) distance of expected post-plate vertex ( $0 \text{ mm}$ ) at bottom of an edge post/plate junction. Area of enlargement: (L) top edge plate-post vertex (thick gray lines) and bottom edge plate-post vertex (thick gray lines).

seeding density for 100% surface coating was estimated based on cell diameter and scaffold surface area).  $200 \mu\text{L}$  of hMSC infusate was layered onto the scaffolds in a multi-well plate (low-attachment plastic) with a micropipette. The plate was placed in a vacuum chamber which was rapidly pumped down to  $25 \text{ Hg}$  for  $1 \text{ min}$ . The loaded scaffolds were then incubated for  $2 \text{ h}$  to facilitate cell attachment.

At the end of  $2 \text{ h}$ , the wells were filled with culture medium (DMEM-LG with  $10\%$  FBS) to prevent drying. The scaffolds were harvested sequentially at four time intervals -  $6$ ,  $18$ ,  $30$ , and  $48 \text{ h}$ —and fixed with  $1\%$  glutaraldehyde solution for  $30 \text{ min}$ . The fixed samples were then rinsed with and stored in phosphate buffered saline (PBS) at  $4^\circ\text{C}$ .

The scaffolds were later retrieved and rinsed with PBS three times, after which they were immersed in a  $1\%$  osmium tetroxide ( $\text{OsO}_4$ ) solution for  $30 \text{ min}$ . The  $\text{OsO}_4$  solution was removed and the samples were rinsed with distilled water three times. The scaffolds were then dehydrated using a graded ethanol series consisting of  $50\%$ ,  $70\%$ ,  $95\%$ , and  $100\%$  ethanol. The samples were immersed three times in each grade for a period of  $5 \text{ min}$  each. The scaffolds were then transferred (in  $100\%$  ethanol) to a BAL-TEC CPD 030 critical point drying device (CPD) (Leica Microsystems, Buffalo Grove, IL). The ethanol was exchanged with liquid  $\text{CO}_2$ , which was used as the medium for the CPD process. Once dry, the

samples were sputter coated with Pd and images were collected using a Quanta<sup>TM</sup> 3D 200 scanning electron microscope (FEI Company, Hillsboro, OR).

### 2.9. Canine MSC seeding and bioreactor culturing

Five PPF scaffolds were placed into a perfusion bioreactor system (figure 5). Each scaffold was loaded with  $2 \text{ million}$  canine MSCs (cMSCs) in  $200 \mu\text{L}$  of DMEM-LG supplemented with  $10\%$  FBS. A vacuum was used to draw the dense infusate into the scaffold pore space. The scaffolds were incubated without flow for a period of  $2 \text{ h}$  to provide sufficient time for cell attachment. After  $2 \text{ h}$ , a continuous  $50 \mu\text{L h}^{-1}$  flow of fresh media (i.e., no media recycling) was used to perfuse the constructs. After seven days of bioreactor culturing, scaffolds were removed and processed for SEM imaging as described above.

## 3. Results

### 3.1. $\text{TiO}_2$ /BAPO dye-initiator package calibration

We have determined that overcuring values in the  $70 \mu\text{m}$  range is useful for accurately rendering scaffolds with  $50 \mu\text{m}$  thick layers [10]. Thus, we polymerize  $120 \mu\text{m}$  thick layers while



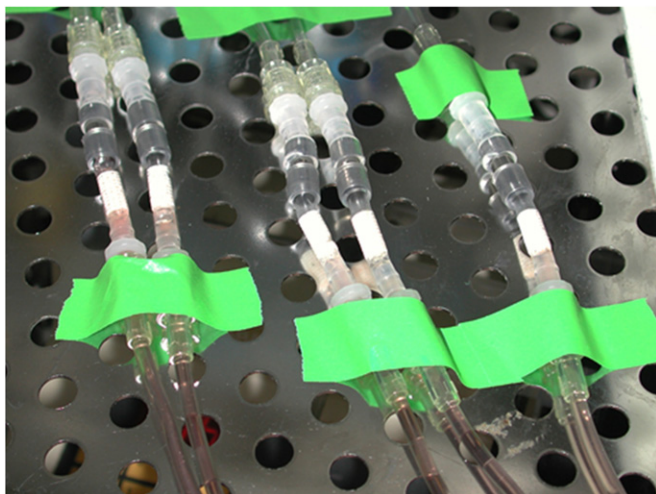


**Figure 5.** Bioreactor culturing of full-sized scaffolds: five full-sized scaffolds, following MSC-seeding and cell attachment, can be seen inside of these bioreactors fabricated in the Department of Biology at Case Western Reserve University (Cleveland, OH). Syringe pumps are used to control the flow of nutrients and growth factors through each bioreactor.

advancing the build platform 50  $\mu\text{m}$  between the rendering of each layer.

### 3.2. Post-cured specimen mechanical properties

Our uniaxial compression tests of 10 mm diameter, 20 mm tall cylinders presented an average modulus of  $135 \pm 8$  MPa ( $N = 5$ ).

### 3.3. Test scaffold accuracy

The diameters of four 2-plate test scaffolds (figure 3(A)) were measured with digital calipers and those measurements are reported in table 1. The average plate diameter was 5.92 mm, 80  $\mu\text{m}$  (13%) less than the target diameter of 6 mm, standard deviation 70  $\mu\text{m}$  (12%), and approximately double the Perfactory P3 device's native XY resolution limit (i.e., 42  $\mu\text{m}$ ) or three times the resolution of our digital calipers (25.4  $\mu\text{m}$ ) [40].

### 3.4. Full-size scaffold rendering accuracy

The rendering accuracy of 16 full-size (i.e., 11-plate) scaffolds was studied via SEM (figure 6) and  $\mu\text{CT}$ . A study of segmentation precision (i.e., repeatability of segmentation) was done. Intra-operator segmentation reliability of was tested by comparing the first and second attempts of a single operator five times. Inter-operator segmentation reliability was tested by comparing five images segmented by the first operator with the same five images segmented by a second operator. Average features of all three types varied between 0.89 and 1.03% both within and between the two segmentation operators. Therefore, segmentation was assumed to be reliable. One operator collected all of the linear distance, curvature, and perpendicular bisector measurements.

Accuracy, with respect to the target value, was calculated as a root mean square error (RMSE):  $\sqrt{1/n \sum_{i=1}^n (o_i - t_0)^2}$ , where  $t_0$  is the target value and  $o_i$  is the observed  $i$ th sample value. When the target value was not equal to zero, a modified coefficient of variation (mCV) was also calculated as RMSE/target. Both RMSE and mCV are very small and hence indicate excellent accuracy. In addition to these overall measurements of accuracy, figure 7 provides histograms of the samples in reference to their target values (shown as a vertical red line), revealing directional information on small discrepancies which are informative for further accuracy improvement. It is clear that from the first, third, fifth, and sixth histograms of figure 7, the plate and pore curvatures, perpendicular bisector, and thickness overshoot a bit from the targets, while the post curvature is peaked at the target but has some very small values, and scaffold lengths tend to undershoot the target (12.4 mm) a small amount.

The average linear distance measurements of overall scaffold length, expected to be 12.4 mm, was observed to be 11.75 mm, with a RMSE of 0.672 mm and mCV of 5.4%, which is much smaller than 20%. The average plate thickness, expected to be 400  $\mu\text{m}$ , observed was 450  $\mu\text{m}$ , with a RMSE of 6.2  $\mu\text{m}$  and mCV of 15.5%. Plate thickness measurements taken in the center of the scaffold were thicker than those taken on the outer edge ( $p = 3.17 \times 10^{-15}$ ).

The average curvature measurement of scaffold plates, expected to be  $0.333 \text{ mm}^{-1}$ , observed was  $0.350 \text{ mm}^{-1}$  with RMSE of  $0.019 \text{ mm}^{-1}$  and mCV of 5.8%. The average curvature measurement of scaffold posts, expected to be  $3.33 \text{ mm}^{-1}$ , observed was  $2.97 \text{ mm}^{-1}$  with a RMSE of  $0.4 \text{ mm}^{-1}$  and mCV of 12.6%. The average curvature measurement of scaffold pores, expected to be  $2.50 \text{ mm}^{-1}$ , observed was  $3.33 \text{ mm}^{-1}$  with a RMSE of  $0.895 \text{ mm}^{-1}$  and mCV of 35.8%.

The average perpendicular bisector of the angle between plates and posts at the edge at the top of scaffolds, expected to be 0, was observed to be 0.41 mm with a RMSE of  $0.47 \text{ mm}^{-1}$  (table 2). No difference was seen when the angle was measured in the top-left, top-right, bottom-left or bottom-right interfaces of the scaffold ( $p = 0.829$ ).

### 3.5. In Vitro test of human MSC (hMSC) attachment

The SEM images shown in figure 8 demonstrate the results of seeding full-size scaffolds with hMSCs. The scaffolds shown in this figure were fixed at 6, 18, 30, and 48 h. They show attached cells progressively flattening at early time points. At later time points these cells have coated the PPF surface and begun the secretion of extracellular matrix (ECM).

### 3.6. Bioreactor culturing of canine MSCs (cMSCs) on PPF scaffolds

After seven days of perfusion bioreactor culturing, flattened cMSCs were observed to fully coat the scaffold surface. One of the constructs was cut to allow for visualization of the cross-section. Analysis of the scaffold border revealed that a coating approximately 9  $\mu\text{m}$  thick had covered the scaffold (figure 9(B)). We expect that this coating is bone extracellular

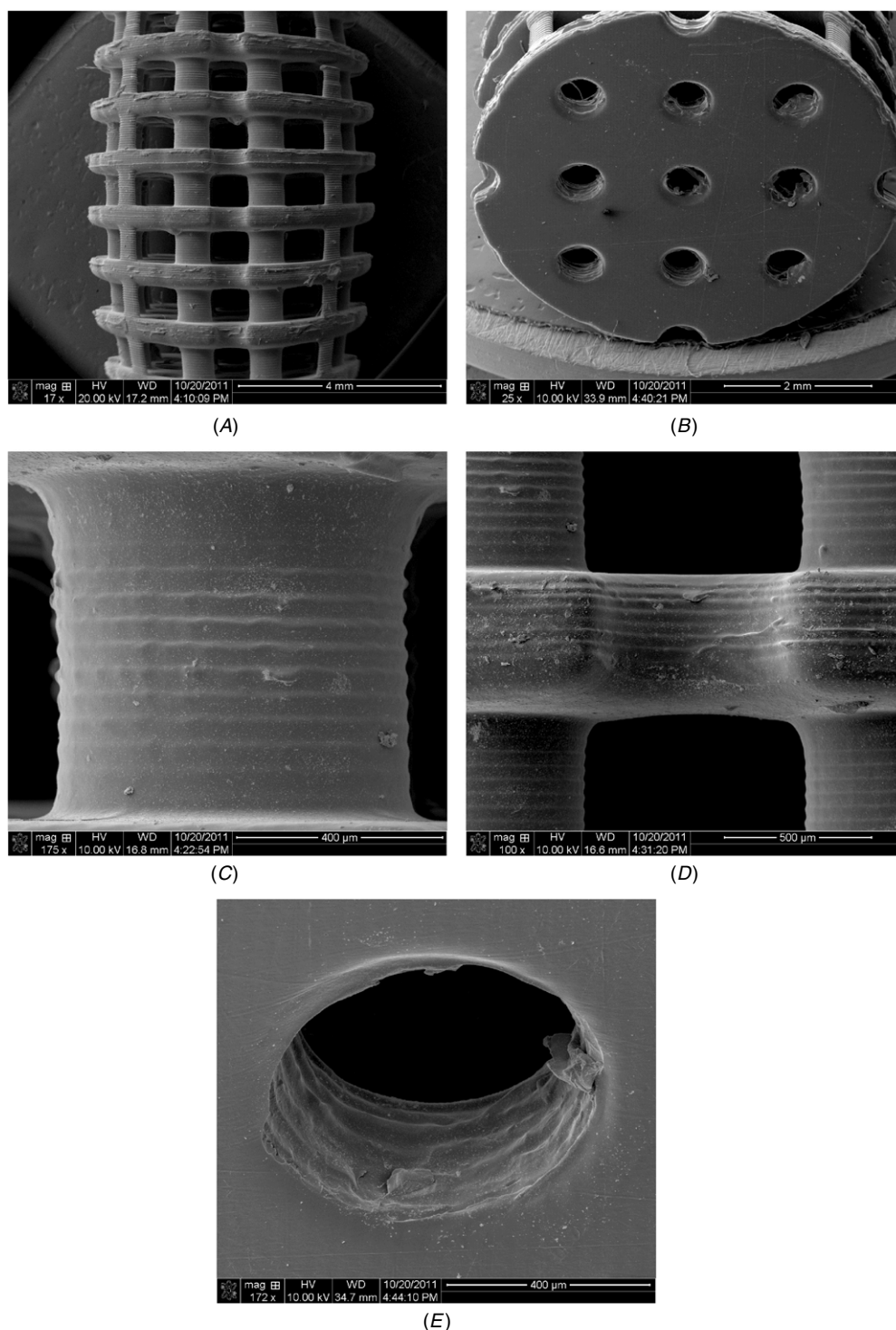


**Figure 6.** SEM images illustrating rendered scaffold accuracy. (A) Side view of the scaffold (note the presence of barrel distortion, i.e., ‘fisheye’ distortion, at low magnification) (17X). (B) Scaffold top surface as seen from an oblique viewpoint (25X). Higher magnification detailed views of (C) scaffold post (175X), (D) scaffold plate (100X), and (E) circular vertical pore (172X). Note that (E) is viewed in an oblique orientation.

matrix; however this was not histologically verified. It should be noted that no growth factors were used to promote extracellular matrix formation during bioreactor culturing, rather our investigation was limited to whether cells would attach under bioreactor conditions that included media flow of  $50 \mu\text{l h}^{-1}$ .

## 4. Discussion

### 4.1. Post-rendering handling

We determined that final part accuracy is dependent upon thorough part cleaning prior to any post-curing. The choice

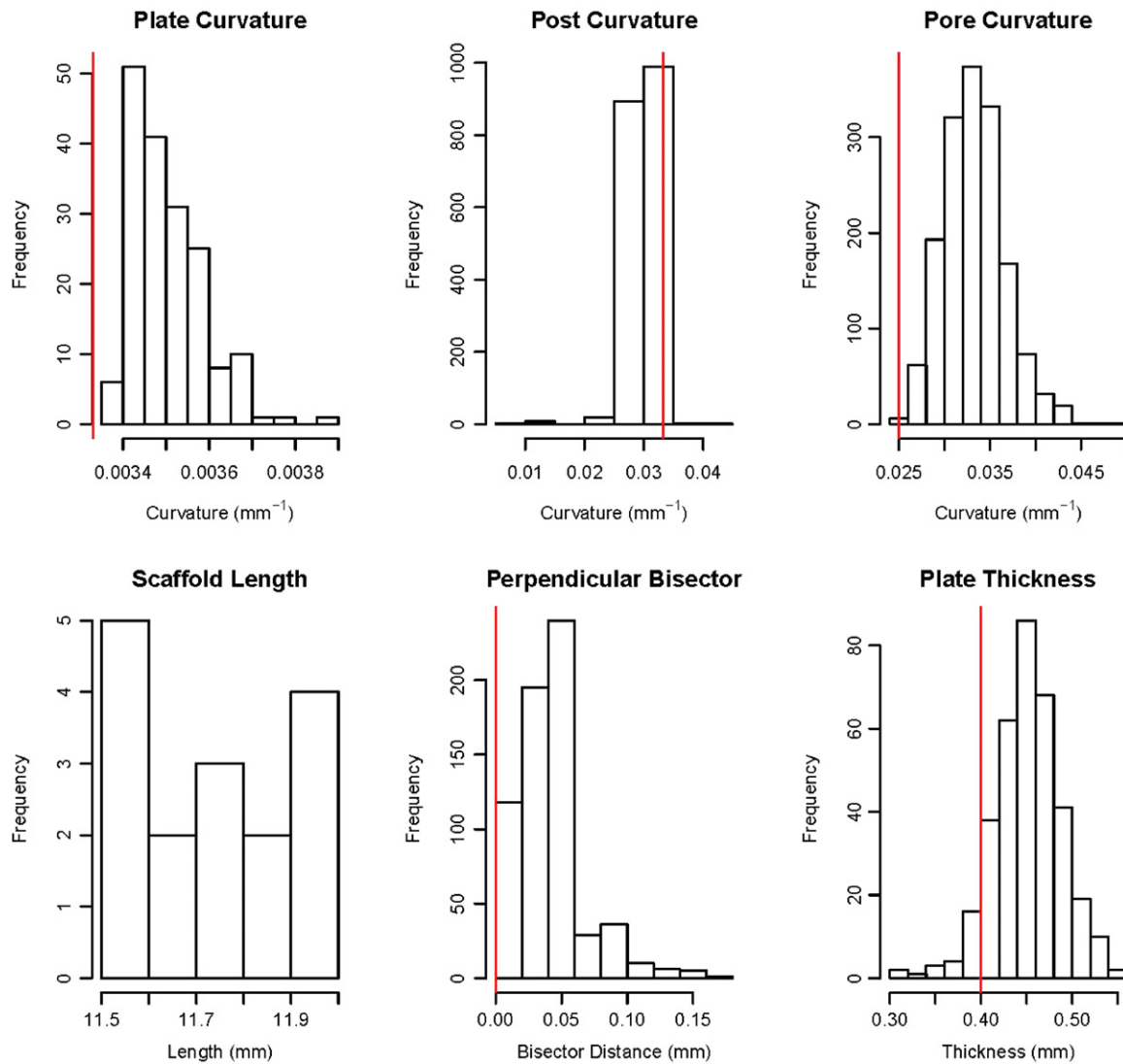


**Figure 7.** Linear and shape measures of accuracy. Linear measures include: scaffold length and plate thickness. Shape measures include: plate curvature, post curvature, pore curvature, and perpendicular bisector. Target values shown as vertical red lines.

**Table 2.** Distance and shape scaffold rendering accuracy ( $\mu$ CT measurements). Full-size scaffold fabrication accuracy: both linear distance (length and thicknesses) and shape measures were collected. The first shape measure, curvature (plate, post, and pore), tested the roundness of round features. The second shape measure, perpendicular bisector (post-edge junction), tested the fabrication of right angles. (N/A = not applicable.)

Measurement (# observations) (unit)	Expected	Average observed	RMSE	mCV (%)
Scaffold length (16) (mm)	12.4 mm	11.75 mm	0.672 mm	5.4
Plate thickness (372) (micrometer)	400 $\mu$ m	450 $\mu$ m	62.0 $\mu$ m	15.6
Plate curvature (185) ( $\text{mm}^{-1}$ )	0.333 $\text{mm}^{-1}$	0.350 $\text{mm}^{-1}$	0.019 $\text{mm}^{-1}$	5.8
Post curvature (2024) ( $\text{mm}^{-1}$ )	3.33 $\text{mm}^{-1}$	2.97 $\text{mm}^{-1}$	0.42 $\text{mm}^{-1}$	12.6
Pore curvature (1672) ( $\text{mm}^{-1}$ )	2.50 $\text{mm}^{-1}$	3.33 $\text{mm}^{-1}$	0.89 $\text{mm}^{-1}$	35.7
Perpendicular bisector top edge (676) (mm)	0.0 mm	0.41 mm	0.49 $\text{mm}^{-1}$	N/A

Note: expected, average observed, and RMSE are in the same units;  $\text{mCV} = \text{RMSE}/\text{target}$ ; mCV is acceptable or 'equivalent to the target' if  $\text{mCV} \leq 20\%$ .

of washing procedures relies on the mechanical integrity of the curing level of the resin produced by the Perfactory additive manufacturing procedure (i.e., before post-curing), often referred to as its 'green strength' [41]. Once cleaned, we found that final part strength was improved by post-curing in a UV bath.

#### 4.2. Rendering accuracy

Our current rendering method is highly accurate (see section 3.3); however, while high, the level of accuracy is not invariant. That is why we compared linear measurements separately from measurements of geometric (shape) accuracy.

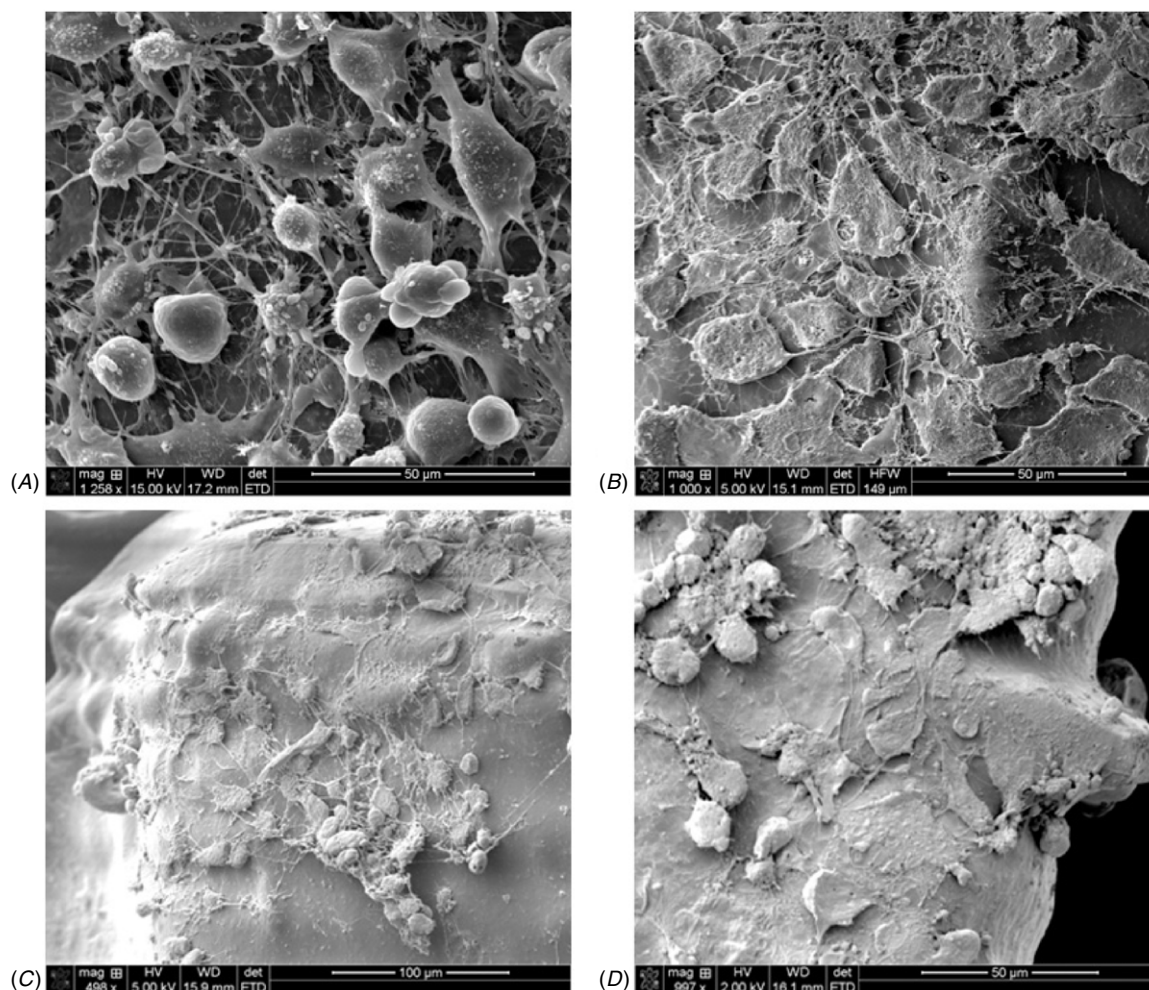


**Figure 8.** SEM images of PPF scaffolds seeded with human mesenchymal stem cell and fixed after (A) 6 h, (B) 18 h, (C) 30 h, and (D) 48 h. These images show cell attachment and progressive spreading, and subsequent coating of the scaffold surface, presumably with bone extracellular matrix.

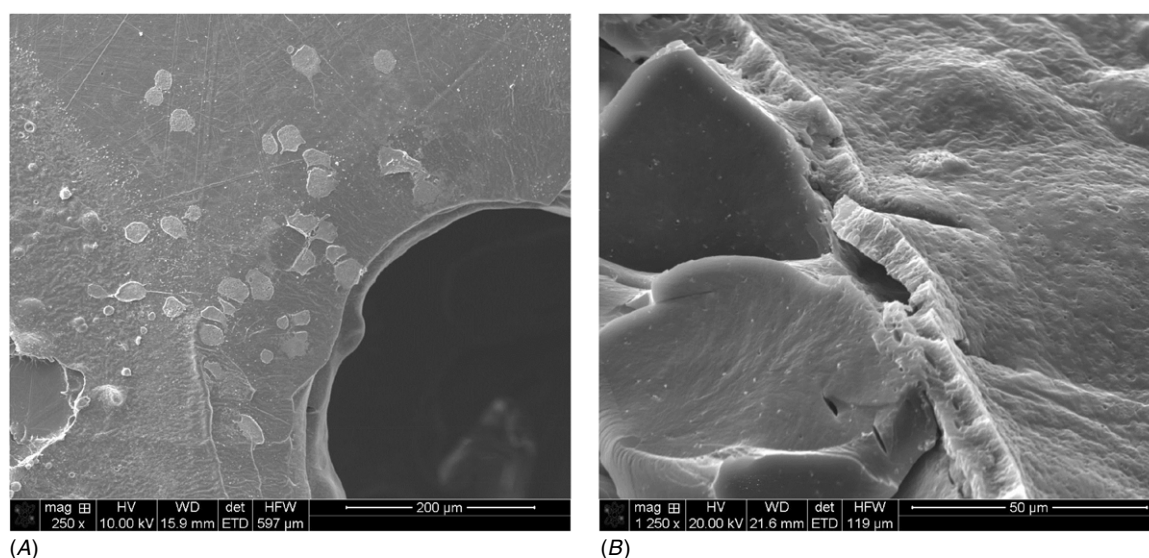


**Figure 9.** SEM images of PPF scaffolds seeded with canine MSCs and conditioned for seven days in a perfusion bioreactor. (A) Cells are visible on the scaffold surface, verifying that attachment was not disrupted by flow. (B) A cross-section of a scaffold sample. Cutting the sample allowed measurement of the presumed ECM coating's thickness. It is clear that this coating had formed external to the PPF surface. The coating is approximately 9  $\mu\text{m}$  thick.



There are at least three sources of error that we found affect linear and geometric accuracies differently. The four sources of error are: (1) native device 3D printing resolution, (2) inadvertent photo-polymerization or 'dark curing', (3) uncompensated overcuring between layers, and (4) post-curing polymer shrinkage.

As expected, shrinkage was not isotropic. Support structures are not only used to allow removal of the rendered part from the burn-in patch. Without supports, areas of the part that are largely attached to the burn-in patch would be less able to shrink than areas further away from the burn-in patch. This phenomenon is seen on a smaller scale within the part. Areas of posts near the plates are less able to shrink than central areas of the post, producing a mild thinning of the posts centrally. This same phenomenon results in a rounding of the junction between plates and posts, a phenomenon that we tried to capture with our perpendicular bisector measurements. Similarly, internal areas of plates are less able to shrink than external areas. Thus, shrinkage anisotropy is seen as less shrinkage in larger or affixed structures. Shrinkage can be compensated for in design software. It can also be reduced by using higher molecular weight polymers [42], however using high molecular weight polymers may reduce the ability of the material to resorb at the correct time.

The dark cure resulting from the use of TiO<sub>2</sub> is seen as inadvertent curing of polymer that we remove from the resin by straining; however, it is also found in the spanning of small gaps at the surface or in the porous internal architecture. In the full scaffolds rendered in the study, this is best illustrated by the 35.8% error in pore curvature. We expect that the large decrease in the diameter of these pores owes to the fact that they are within the XY plane where the effect of TiO<sub>2</sub> light scattering (i.e., dark cure) should be strongest because they are completely parallel to the build plane. This phenomenon could be compensated for in the design software or, possibly, eliminated by using less of TiO<sub>2</sub> or a dye that does not scatter light in directions oblique to Z.

#### 4.3. Pre-culturing of implants in a perfusion bioreactor system

Implant pre-culturing may allow for the production of a construct which is already coated with an osteoconductive extracellular matrix prior to implantation. The presence of cells after seven days of continuous flow demonstrated that cells can attach and remain attached to these cDLP-rendered PPF scaffolds under these conditions. A coating which formed over the scaffold surfaces was observed and is suspected to have secreted bone extracellular matrix (ECM). Additional characterization will be necessary to verify our hypothesis that this coating is bone ECM. We expect that the use of growth factors, the suppletion of minerals relevant to bone ECM, and that shear stress resulting from flow, will allow the thickness and composition of this ECM coating to be tuned.

## 5. Conclusions

This work has demonstrated the use of cDLP as an additive manufacturing technique suitable for the production of highly

accurate, porous polymer scaffolds. In combination with patient image data (e.g., from a 3D computed tomography scan), this technique could be used to produce scaffolds which accurately fit a patient defect site. The high resolution available with cDLP also allows for the production of accurate pore geometries with appropriate orientation, and in theory could also be used to generate surface features at a scale detectable to cells (i.e., roughness features). Thus, factors at each of the three scale spaces discussed above—cell-scaffold, scaffold-tissue, and tissue-organ—can be part of the scaffold design strategy with this technique, thereby providing a powerful set of tools for biofabrication. The PPF scaffolds produced in this study were suitable for cMSC and hMSC attachment. Preliminary results of bioreactor pre-culturing suggest that it will be possible to coat MSC-loaded, cDLP-rendered PPF implants with ECM prior to implantation, providing an osteoconductive surface on implantation rather than relying on the *in vivo* environment of the wound to recruit and coat the PPF bone tissue engineering scaffold with new tissue [43, 44].

## Acknowledgments

This manuscript was significantly improved by reviewer comments. This research was partially supported by the Research Foundation of the Department of Neurological Surgery, Case Western Reserve University (CWRU), Cleveland, OH and by NIH grant R01-DE013740. The images shown in figures 6, 8, and 9 were taken at the Swagelok Center for Surface Analysis of Materials (SCSAM) at CWRU. The  $\mu$ CT characterization was performed under the guidance of Dr Maureen L Dreher, Division of Solid and Fluid Mechanics, Office of Science and Engineering Laboratories, Center for Devices and Radiological Health at the Food and Drug Administration. We are grateful to Dr Antonios G Mikos, Department of Bioengineering, Rice University (Houston, TX) for helpful comments on this study and manuscript. We are grateful to Dr Steven Eppell, Department of Biomedical Engineering, CWRU for providing us access to a critical point drying device. We thank Jay Bensusan who assisted with the compression testing which was performed in Dr Clare Rimnac's laboratory, Department of Mechanical and Aerospace Engineering, CWRU. We also wish to thank Eric Mott, Department of Neurological Surgery, CWRU, who generated figure 2(B). We are grateful to Jim Berilla, Department of Civil Engineering, CWRU, who machined the tooling for, and built, the bioreactors used in this projects.

## References

- [1] ASTM Standard Terminology For Additive Manufacturing Technologies 2013 ASTM F2792-12a (*West Conshohocken, PA: American Society for Testing and Materials*) [www.astm.org/Standards/F2792.htm](http://www.astm.org/Standards/F2792.htm) (last accessed 4 November 2013)
- [2] Adachi T, Osako Y, Tanaka M, Hojo M and Hollister S J 2006 Framework for optimal design of porous scaffold microstructure by computational simulation of bone regeneration *Biomaterials* **27** 3964–72

- [3] Almeida H A and Bártolo P J 2010 Virtual topological optimisation of scaffolds for rapid prototyping *Med. Eng. Phys.* **32** 775–82
- [4] Kim K, Dean D, Wallace J, Breithaupt R, Mikos A G and Fisher J P 2011 The influence of stereolithographic scaffold architecture and composition on osteogenic signal expression with rat bone marrow stromal cells *Biomaterials* **32** 3750–63
- [5] Schmitz J P and Hollinger J O 1986 The critical size defect as an experimental model for craniomandibulofacial nonunions *Clin. Orthop. Relat. Res.* **205** 299–308
- [6] Cooke M N, Fisher J P, Dean D, Rimnac C and Mikos A G 2003 Use of stereolithography to manufacture critical-sized 3D biodegradable scaffolds for bone ingrowth *J. Biomed. Mater. Res. B* **64** 65–69
- [7] Dean D, Wallace J, Kim K, Mikos A G and Fisher J P 2010 Stereolithographic Rendering of low molecular weight polymer scaffolds for bone tissue engineering *Innovative Developments in Design and Manufacturing: Advanced research in virtual and rapid prototyping: Proc. 4th Int. Conf. on Advanced Research and Rapid Prototyping (Leiria, Portugal, 6–10 Oct. 2009)* ed P J Bártolo et al (Boca Raton, FL: CRC Press) pp 37–43
- [8] Jansen J, Melchels F P, Grijpma D W and Feijen J 2009 Fumaric acid monoethyl ester-functionalized poly(D,L-lactide)/N-vinyl-2-pyrrolidone resins for the preparation of tissue engineering scaffolds by stereolithography *Biomacromolecules* **10** 214–20
- [9] Dean D, Wallace J, Siblani A, Wang M O, Kim K, Mikos A G and Fisher J P 2012 The calibration of continuous digital light processing (cDLP) for the highly accurate additive manufacturing of tissue engineered bone scaffolds *Innovative Developments in virtual and Physical Prototyping: Proc. 5th Int. Conf. on Advanced Research in Virtual and Rapid Prototyping (Leiria, Portugal, 28 Sept.–1 Oct. 2011)* ed P J Bártolo et al (Boca Raton, FL: CRC Press) pp 57–66
- [10] Dean D, Wallace J, Siblani A, Wang M O, Kim K, Mikos A G and Fisher J P 2012 Continuous digital light processing (cDLP): highly accurate additive manufacturing of tissue engineered bone scaffolds *Virtual Phys. Prototyping* **7** 13–24
- [11] Fisher J P, Dean D and Mikos A G 2002 Photocrosslinking characteristics and mechanical properties of diethyl fumarate/poly(propylene fumarate) biomaterials *Biomaterials* **23** 4333–43
- [12] Sankara S and Gopchandran K G 2013 Rutile TiO<sub>2</sub>(101) based plasmonic nanostructures *Ceram. Int.* **39** 1081–6
- [13] Fisher J P, Dean D, Engel P S and Mikos A G 2001 Photoinitiated polymerization of biomaterials *Annu. Rev. Mater. Res.* **31** 171–81
- [14] Fisher J P, Timmer M D, Holland T A, Dean D, Engel P S and Mikos A G 2003 Photoinitiated cross-linking of the biodegradable polyester poly(propylene fumarate): part I. Determination of network structure *Biomacromolecules* **4** 1327–34
- [15] [www.sachtleben.de/index.php?id=145](http://www.sachtleben.de/index.php?id=145) (last accessed August 10, 2013)
- [16] Chung C J, Su R T, Chu H J, Chen H T, Tsou H K and He J L 2013 Plasma electrolytic oxidation of titanium and improvement in osseointegration *J. Biomed. Mater. Res. B* **101** 1023–30
- [17] Timmer M D, Shin H, Horch R A, Ambrose C G and Mikos A G 2003 *In vitro* cytotoxicity of injectable and biodegradable poly(propylene fumarate)-based networks: unreacted macromers, cross-linked networks, and degradation products *Biomacromolecules* **4** 1026–33
- [18] Wang M O, Etheridge J M, Thompson J A, Vorwald C E, Dean D and Fisher J P 2013 Evaluation of the *in vitro* cytotoxicity of cross-linked biomaterials *Biomacromolecules* **14** 1321–29
- [19] Melchels F P, Tonnarelli B, Olivares A L, Martin I, Lacroix D, Feijen J, Wendt D J and Grijpma D W 2011 The influence of the scaffold design on the distribution of adhering cells after perfusion cell seeding *Biomaterials* **32** 2878–84
- [20] Kroeze R J, Helder M N, Roos W H, Wuite G J, Bank R A and Smit T H 2010 The effect of ethylene oxide, glow discharge and electron beam on the surface characteristics of poly(L-lactide-co-caprolactone) and the corresponding cellular response of adipose stem cells *Acta Biomater.* **6** 2060–5
- [21] Chim H, Ong J L, Schantz J T, Huttmacher D W and Agrawal C M 2003 Efficacy of glow discharge gas plasma treatment as a surface modification process for three-dimensional poly (D,L-lactide) scaffolds *J. Biomed. Mater. Res. A* **65** 327–35
- [22] Zhao G, Raines A L, Wieland M, Schwartz Z and Boyan B D 2007 Requirement for both micron- and submicron scale structure for synergistic responses of osteoblasts to substrate surface energy and topography *Biomaterials* **28** 2821–9
- [23] Fini M, Giardino R, Borsari V, Torricelli P, Rimondini L, Giavaresi G and Nicoli Aldini N 2003 *In vitro* behaviour of osteoblasts cultured on orthopaedic biomaterials with different surface roughness, uncoated and fluorohydroxyapatite-coated, relative to the *in vivo* osteointegration rate *Int. J. Artif. Organs* **26** 520–8
- [24] Kim K, Dean D, Lu A, Mikos A G and Fisher J P 2011 Early osteogenic signal expression of rat bone marrow stromal cells is influenced by both hydroxyapatite nanoparticle content and initial cell seeding density in biodegradable nanocomposite scaffolds *Acta Biomater.* **7** 1249–64
- [25] Park J S, Chu J S, Tsou A D, Diop R, Tang Z, Wang A and Li S 2011 The effect of matrix stiffness on the differentiation of mesenchymal stem cells in response to TGF- $\beta$  *Biomaterials* **32** 3921–30
- [26] Burke D P and Kelly D J 2012 Substrate stiffness and oxygen as regulators of stem cell differentiation during skeletal tissue regeneration: a mechanobiological model *PLoS One* **7** e40737
- [27] Song M J, Dean D and Knothe Tate M L 2010 *In situ* spatiotemporal mapping of flow fields around seeded stem cells at the subcellular length scale *PLoS One* **5** e12796
- [28] Song M J, Brady-Kalnay S M, McBride S H, Phillips-Mason P, Dean D and Knothe Tate M L 2012 Mapping the mechanome of live stem cells using a novel method to measure local strain fields *in situ* at the fluid-cell interface *PLoS One* **7** e43601
- [29] Bos R R M, Rozema F R, Boering G, Nijenhuis A J, Pennings A J, Verwey A B, Nieuwenhuis P and Jansen H W 1991 Degradation of and tissue reaction to biodegradable poly(L-lactide) for use as internal fixation of fractures: a study in rats *Biomaterials* **12** 32–36
- [30] Agrawal C M, Kennedy M E and Micallef D M 1994 The effects of ultrasound irradiation on a biodegradable 50-50% copolymer of polylactic and polyglycolic acids *J. Biomed. Mater. Res.* **28** 851–9
- [31] Peter S J, Miller S T, Zhu G, Yasko A W and Mikos A G 1998 *In vivo* degradation of a poly(propylene fumarate)/beta-tricalcium phosphate injectable composite scaffold *J. Biomed. Mater. Res.* **41** 1–7
- [32] Hollister S J 2005 Porous scaffold design for tissue engineering *Nature Mater.* **4** 518–24
- [33] Anderson E J and Knothe Tate M L 2007 Design of tissue engineering scaffolds as delivery devices for mechanical

- and mechanically modulated signals *Tissue Eng.* **13** 2525–38
- [34] Melchels F P, Barradas A M, van Blitterswijk C A, de Boer J, Feijen J and Grijpma D W 2010 Effects of the architecture of tissue engineering scaffolds on cell seeding and culturing *Acta Biomater.* **6** 4208–17
- [35] Dean D, Min K-J and Bond A 2003 Computer aided design of pre-fabricated cranial plates *J. Craniofac. Surg.* **14** 819–32
- [36] Kasper F K, Tanahashi K, Fisher J P and Mikos A G 2009 Synthesis of poly(propylene fumarate) *Nature Protoc.* **4** 518–25
- [37] Cooke M N 2004 Novel stereolithographic manufacture of biodegradable bone tissue scaffolds *PhD Dissertation* Department of Mechanical and Aerospace Engineering, Case Western Reserve University, Cleveland, OH
- [38] Fisher J P, Holland T A, Dean D, Engel P S and Mikos A G 2001 Synthesis and properties of photocross-linked poly(propylene fumarate) scaffolds *J. Biomater. Sci. Polym. Ed.* **12** 673–87
- [39] Fisher J P, Dean D and Mikos A G 2002 Photocrosslinking characteristics and mechanical properties of diethyl fumarate/poly(propylene fumarate) biomaterials *Biomaterials* **23** 4333–43
- [40] [www.mitutoyo.com/TerminalMerchandisingGroup.aspx?group=1381](http://www.mitutoyo.com/TerminalMerchandisingGroup.aspx?group=1381) (accessed January 22 2013)
- [41] Jacobs P F 1992 *Rapid Prototyping & Manufacturing: Fundamentals of Stereolithography* (Dearborn, MI: Society of Manufacturing Engineers) pp 36–38
- [42] Heller C, Schwentenwein M, Russmueller G, Varga F, Stampfl J and Liska R 2009 Vinyl esters: low cytotoxicity monomers for the fabrication of biocompatible 3D scaffolds by lithography based additive manufacturing *J. Polym. Sci. A* **47** 6941–54
- [43] Dean D et al 2003 Poly(propylene fumarate) and poly(DL-lactic-co-glycolic acid) as scaffold materials for solid and foam-coated composite tissue-engineered constructs for cranial reconstruction *Tissue Eng.* **9** 495–504
- [44] Dean D et al 2005 Effect of transforming growth factor  $\beta_2$  on marrow-infused foam poly(propylene fumarate) tissue-engineered constructs for the repair of critical-size cranial defects in rabbits *Tissue Eng.* **11** 923–39